Supplement of Atmos. Meas. Tech., 16, 209–233, 2023
https://doi.org/10.5194/amt-16-209-2023-supplement

Atmospheric Measurement Techniques
Open Access
EGU

Supplement of

Optical receiver characterizations and corrections for ground-based and airborne measurements of spectral actinic flux densities

Birger Bohn and Insa Lohse

Correspondence to: Birger Bohn (b.bohn@fz-juelich.de)

S1 Zeppelin setup

The actinic radiation receiver setup on the Zeppelin NT is shown schematically in Fig. S1. The two receivers were parallel within $\pm 1°$. No typical pitch angle was compensated for by the mountings but construction-conditioned both receivers were slightly tilted forward by $1.5° \pm 1.0°$ with respect to the airship waterline. The general arrangement is similar to that on HALO but some details differ. Compare with Fig. 2 and see Sect. 2.1 of the main text for more details.

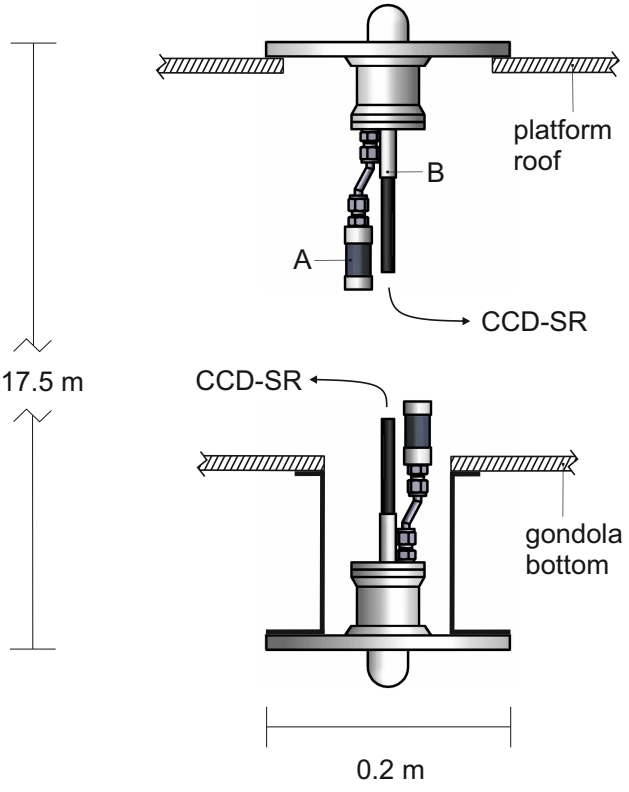

Figure S1. Scheme of the 4π actinic radiation setup on the Zeppelin-NT. The receiver housings were depressurized through 200 μm holes in the drying agent cartridges (A) next to the fibre throughputs (B).

S2 Z_p measurements

S2.1 Laboratory measurements

Photographs of the goniometric setup used for the Z_p determinations are shown in Fig. S2. Ideally, for the Z_p measurements the radiation incident on the receivers should be parallel to avoid any bias related to the receiver geometry. However, technically it is difficult to produce a polychromatic light beam of sufficient extension, intensity and homogeneity. The use of a point light source is therefore more practicable but may require corrections and a carefully adjusted experimental setup. As described in the main text, the position of the equivalent plane of the receivers can change with the polar angle of incidence. Because it would be difficult to readjust the lamp distance during the rotations, the Δz were not determined for different polar angles. Instead Z_p measurements were done at two different distances and the final Z_p were determined by extrapolation to a hypothetical infinite distance where the influence of different Δz vanishes.

If z is the distance between the lamp and the equivalent plane at normal incidence, the measured signals are proportional to the inverse square of z:

$$S(\lambda, \vartheta = 0, \varphi, z) \propto \frac{1}{z^2} \tag{S1}$$

A similar equation applies to other polar angles ϑ:

$$S(\lambda, \vartheta, \varphi, z, \Delta z') \propto \frac{1}{(z + \Delta z')^2} \tag{S2}$$

where the quantity $\Delta z'$ is the difference in Δz:

$$\Delta z'(\vartheta) = \Delta z(\vartheta) - \Delta z(\vartheta = 0) \tag{S3}$$

The measured Z_p correspond to the ratios of Eqns. S2 and S1:

$$Z_\mathrm{p}(\lambda, \vartheta, \varphi, z, \Delta z') = Z_\mathrm{p}^\infty(\lambda, \vartheta, \varphi) \times \{1 + \frac{2\Delta z'}{z} + \frac{\Delta z'^2}{z^2}\}^{-1} \tag{S4}$$

The actual target quantity is Z_p^∞, the Z_p for infinite z when the radiation of the point light source becomes parallel. The equation can be rearranged and further simplified in the case $|\Delta z'| \ll z$:

$$Z_\mathrm{p}^\infty(\lambda, \vartheta, \varphi) \approx Z_\mathrm{p}(\lambda, \vartheta, \varphi, z, \Delta z') \times \{1 + \frac{2\Delta z'}{z}\} \tag{S5}$$

To determine Z_p^∞, measurements were done at two lamp distances, close and far: $z_\mathrm{close} = 400$ mm and $z_\mathrm{far} = 800$ mm. Because a linear dependence is expected for $1/Z_\mathrm{p}$ as a function of $1/z$, a two-point extrapolation towards $1/z = 0$ can be made, resulting in the following equation:

$$Z_\mathrm{p}^\infty(\lambda, \vartheta, \varphi) = \frac{Z_\mathrm{p,far}\, Z_\mathrm{p,close}\{\frac{z_\mathrm{far}}{z_\mathrm{close}} - 1\}}{\frac{z_\mathrm{far}}{z_\mathrm{close}} Z_\mathrm{p,far} - Z_\mathrm{p,close}} \tag{S6}$$

It should be noted that Eqns. S1–S5 are valid if the rotational axis goes through the basis of the receiver's top hemisphere (≈15 mm below the top, see Fig. 1 of main text). If the position of the rotation axis is different, the extrapolation method is still applicable but the definition of $\Delta z'$ differs from that given in Eqn. S3. In practice the rotational axis should go somewhere centrally through the receiver.

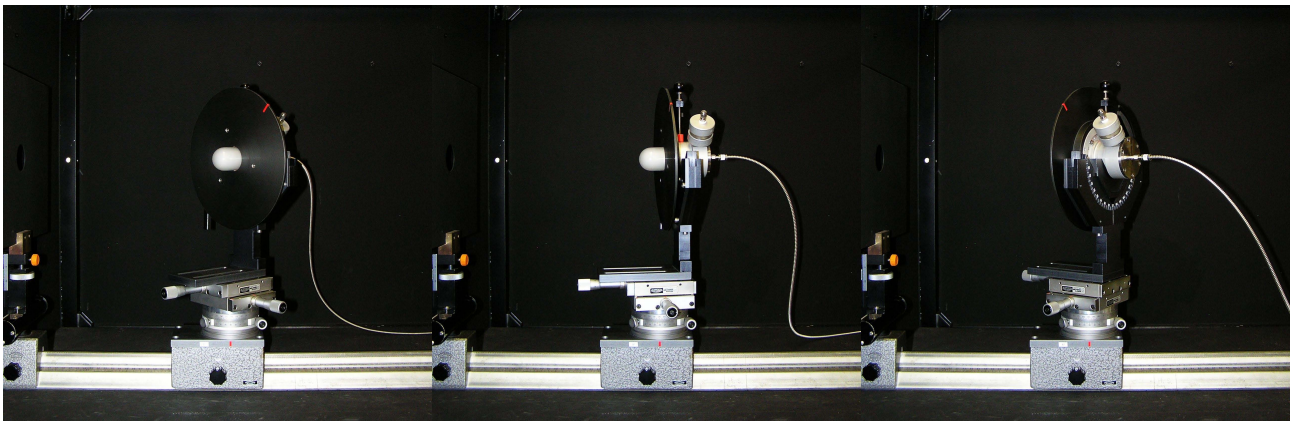

Figure S2. Sequence of three photographs of the goniometric laboratory setup for the determination of Z_{p}. The setting was mounted inside a black box on an optical bench. The lamp was positioned outside the box on the left-hand side behind a blind. The receivers were rotated in two dimensions. Polar and azimuth angles were accurately adjusted, as well as the distances to the lamp and the positions of the rotational axis.

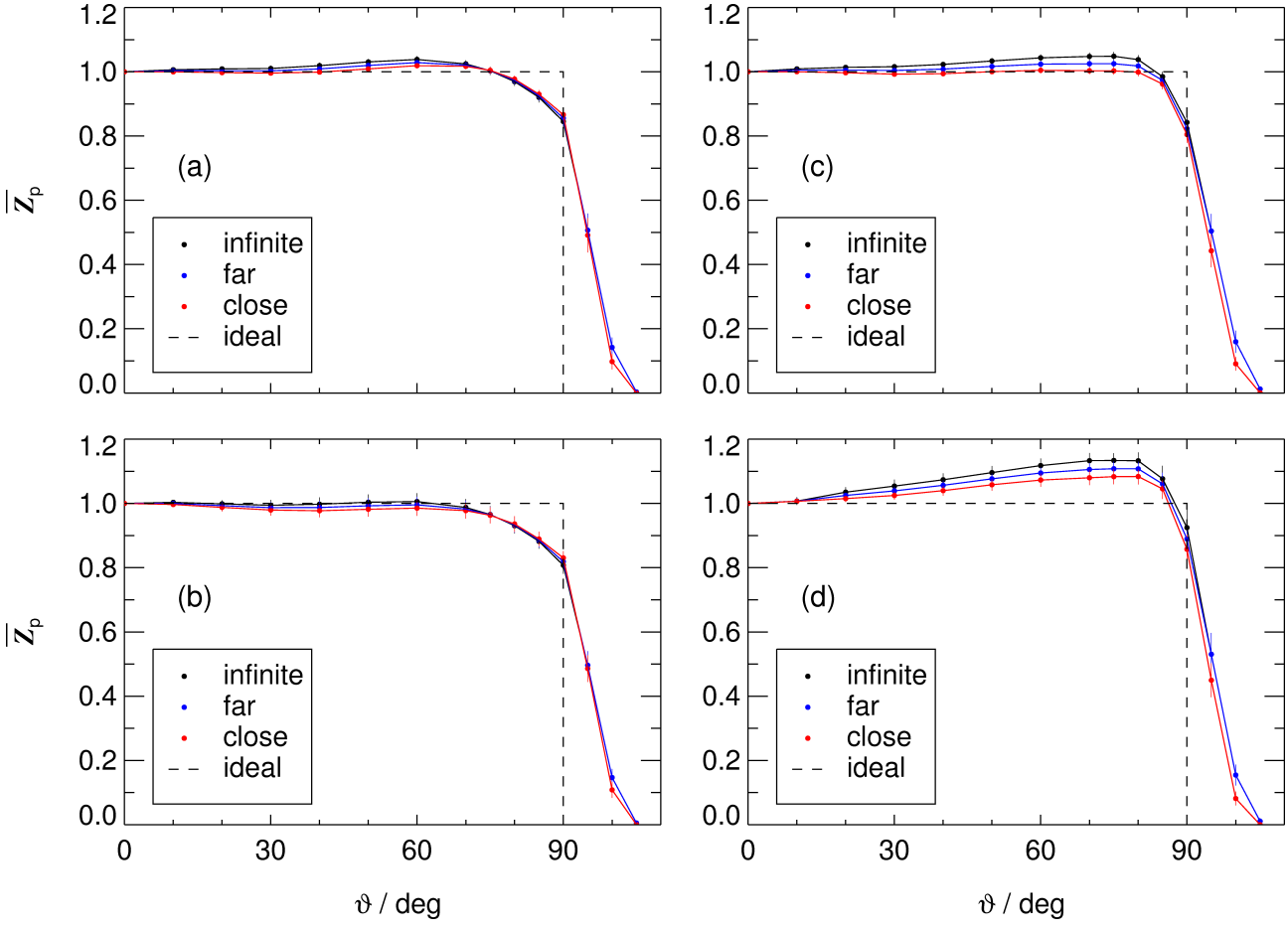

Figure S3. Relative angular sensitivities Z_{p} of HALO and Zeppelin top and bottom receivers for a wavelength of 400 nm at different lamp distances (close, far) and for an extrapolated infinite distance (Eq. S6). (a), (b): HALO top, bottom; (c), (d): Zeppelin top, bottom. Data were averaged over different azimuth angles. Error bars indicate the corresponding standard deviations.

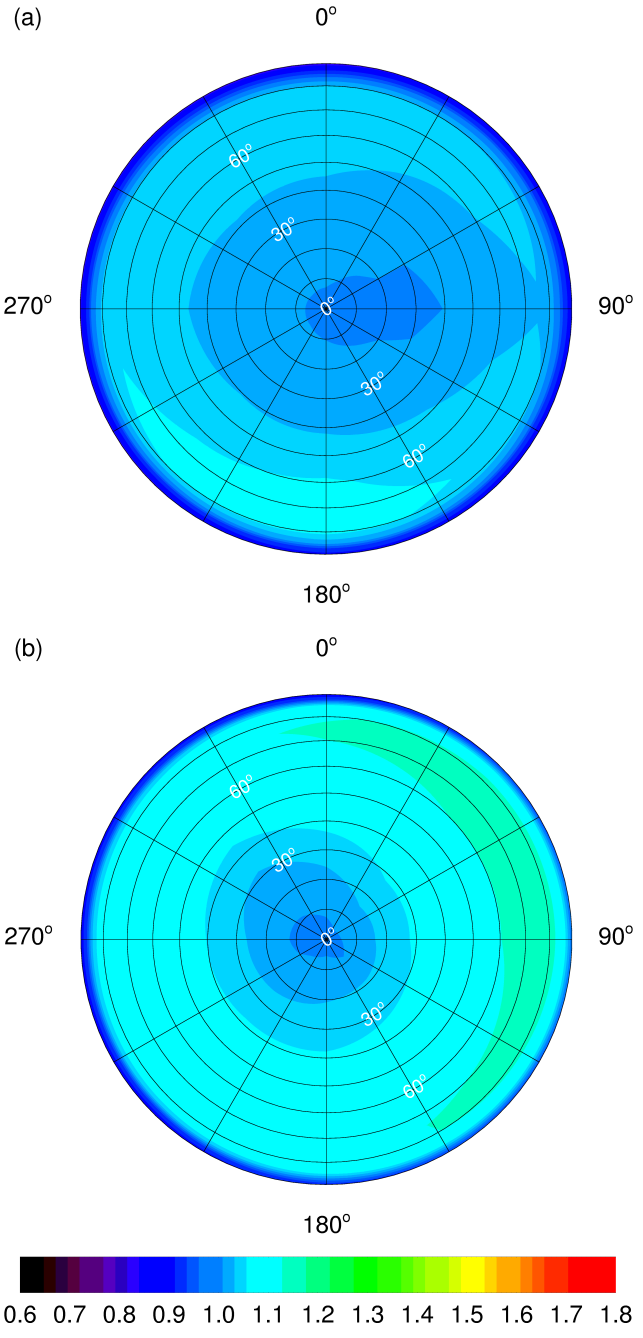

Figure S4. Contour plots of hemispherical relative angular sensitivities Z_p of the Zeppelin 2π (a) top and (b) bottom receivers at 400 nm (top views). Azimuth angles of 0° correspond to flight directions of aircraft-installed receivers. The colour scale was chosen for better comparability with Fig. S12.

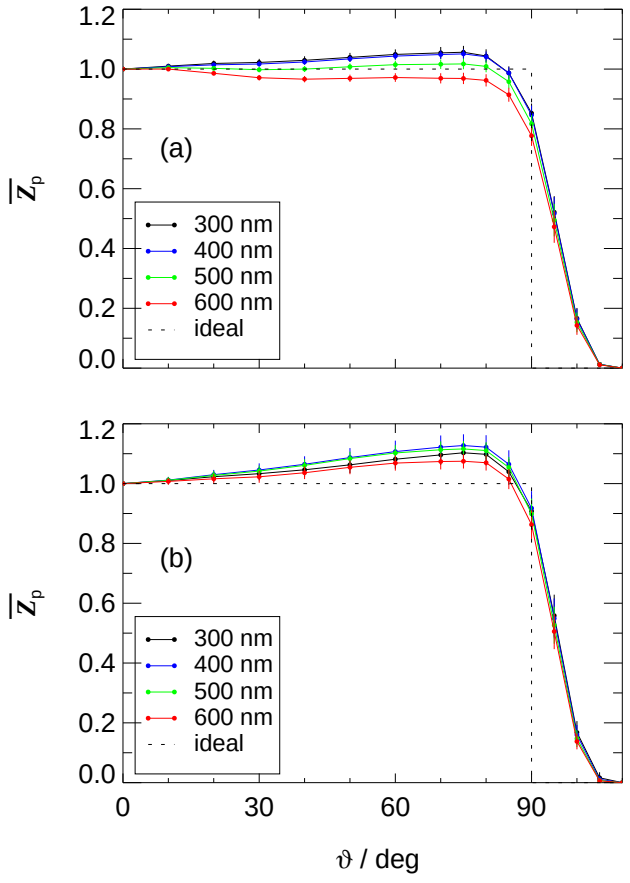

Figure S5. Azimuthal averages of relative angular sensitivities Z_p of Zeppelin (a) top and (b) bottom receivers for selected wavelengths. Error bars indicate standard deviations of the azimuthal variabilities. The relative sensitivity of an ideal 2π receiver is shown for comparison (dashed line). The receivers were built into their original aircraft flanges (Fig. S1).

To keep the $1/z$-dependencies at a minimum, in this work the position of the rotational axis was chosen individually for each receiver, so that the lamp distances to the reference planes were as possible transformed upon rotation from $\vartheta = 0$ to 90°. However, this approach is not necessary and also requires the knowledge of Δz at $\vartheta = 0°$ and 90° (Sect. 3.1). The distances $z_{\mathrm{close}} = 400$ mm and $z_{\mathrm{far}} = 800$ mm were chosen as a compromise. (i) Distances shorter than 400 mm to the hot lamp are difficult to handle and can lead to deviations. (ii) Distances greater than 800 mm result in too small and noisy signals in the UV range. (iii) An extrapolation to $1/z = 0$ from a range (1.25–2.50)$\times 10^{-3}$ mm^{-1} is feasible.

It turned out that for the HALO receivers the z dependence of the measured Z_{p} was small while for the Zeppelin receivers it was more significant. As an example Fig. S3 shows the ϑ dependence of Z_{p} of HALO and Zeppelin receivers for close, far and infinite z for a wavelength of 400 nm. The behaviour for other wavelengths looks similar. However, below about 340 nm the signals at z = 800 mm were too noisy as an input for Eq. S6. Because for longer wavelengths close and far results differed by virtually the same factors, these factors were also applied at smaller wavelengths. For $\vartheta > 90°$ Eq. S6 was also not applied because of a premature shading of receivers by the aircraft flanges at close distances to the point light source. Instead the far measurements were used and multiplied with the wavelength-dependent factor far/infinty at 90°.

The index ∞ for the Z_{p} will be omitted in the following, as well as in the main paper. Contour plots of the finally derived Z_{p} are plotted in Fig. S4 for the Zeppelin top and bottom receivers for a wavelength of 400 nm. Fig. S5 shows azimuthal mean values for these receivers for selected wavelengths where the error bars represent the azimuthal variability (compare with Figs. 4 and 5 of the main text showing the same data for the HALO receivers). Relative uncertainties for the azimuthal averaged Z_{p} were estimated based on the variability and the accuracy of the lab measurements. For wavelengths above 350 nm they gradually increase from 0% at ϑ = 0° (reference measurement) to 4% at ϑ = 90°, 10% at ϑ = 95°, and 20% at ϑ = 100°. For wavelengths below 350 nm these uncertainties were stepwise increased by up to a factor of 1.5 at 300 nm because of the unreliable Z_{p} determinations at z = 800 mm.

S2.2 Field of view effects

A field of view limitation beyond that produced by the aircraft flanges can be caused by the aircraft fuselage and additional mounts. This limitation is usually welcome to repress the cross-talk towards opposite hemispheres. How signals decrease when an increased height of the receiver dome is shaded (from bottom to top) was investigated in the laboratory at $\vartheta = 90°$. The decrease of signals was found to be linear in good approximation. When the shaded area extended to more than 25 mm from the bottom of the receiver (total height ≈ 35 mm) the signals became negligible. For HALO, limiting angles of reception and the corresponding decrease of signals were estimated for different azimuth angles by approximating HALO as an extended cylinder (r = 1.2 m) with a 3.3° tilt in the flight direction with respect to the receiver plane. For the HALO top receiver this results in limiting polar angles ranging between 86.7° in the flight direction, 101.6° in lateral directions and 93.3° against the flight direction. Correspondingly reversed angles apply to the HALO bottom receiver, except for the rearward range where the center wing box and the aircraft wings were limiting the field of view. Because aircraft CAD data were classified, the details were inferred from available technical drawings.

During some deployments (HALO-FLT configuration) the aircraft was equipped with an additional containment at the bottom fuselage that led to further field of view restrictions (S2.4). For the Zeppelin the field of view restrictions of the top receiver (produced by the black roof of the instrument box) were almost ideal (≈ 90.6°) while for the bottom receiver there were no further restrictions, i.e. the Z_{p} data shown in panels (b) of Fig. S4 and S5 apply without further modifications (except for the redefinition of incidence angles for the installed receiver).

S2.3 Fuselage reflections

For the aircraft-installed receivers also the influence of fuselage reflections has to be taken into account. The reflective properties of relevant aircraft surfaces were investigated in the laboratory with a white-painted original flange from HALO and a sample of the black foil used on the roof of the Zeppelin instrument box. Both surfaces exhibited a mixed reflective behaviour with specular and diffuse contributions.

Diffuse reflections at the surfaces were investigated using a special goniometric setup. Angle-dependent spectral radiances of reflected radiation were measured upon normal incidence. The reflectivities were determined using a reflection standard (OptoPolymer) as a reference. The white paint of the HALO flange showed a reflectivity as high as 75% above 400 nm and little dependence on reflection angles in the range ≤70°. On the other hand, below 400 nm the reflectivity decreased strongly to values below 2%. We therefore estimate no significant influence of diffuse reflections on actinic flux density measurements in the UV range (<0.1%). For wavelengths above 400 nm an upper limit of about 1% was estimated for potential enhancements of measured actinic flux densities. The effects are confined by geometrical limitations and low Z_{p} values at relevant incidence angles (ϑ >90°). Because the VIS range is secondary for most photochemical applications, no attempt was made to further specify the influence of the diffuse HALO reflections. The diffuse reflectivity of the black foil on the Zeppelin platform roof turned out to be almost independent of wavelength but strongly dependent on the reflection angle with a reflectivity below 2% at reflection angles ≥70°. Because foil reflected

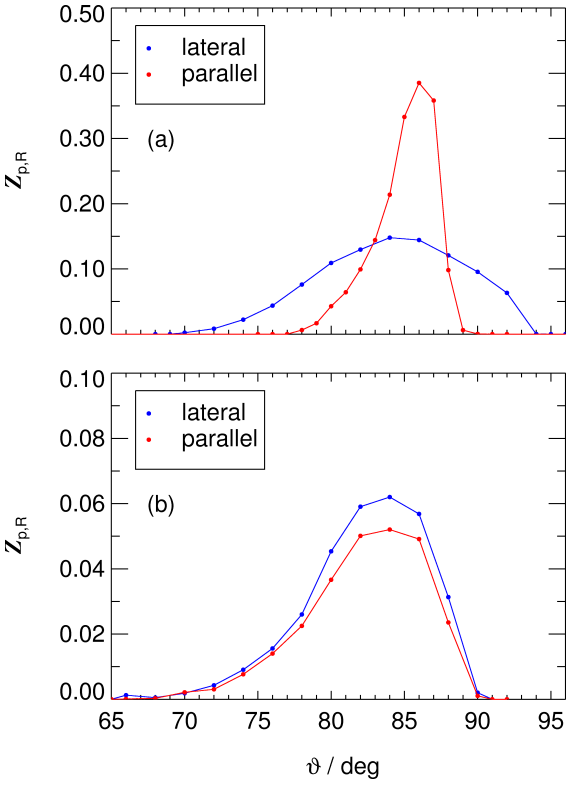

Figure S6. Enhancements $Z_{\mathrm{p,R}}$ of relative angular sensitivities caused by specular reflections on aircraft surfaces. (a) White paint of the HALO fuselage for configurations FLT and FLN. (b) Black plastic foil covering the Zeppelin top platform. The curved shape of the HALO fuselage leads to stronger differences between lateral and parallel incidence with respect to the aircraft longitudinal axis. Data were averaged over a wavelength range 320–420 nm.

radiation at lower angles cannot reach the receiver optics for geometrical reasons, its influence on actinic flux density measurements was estimated negligible (<0.1%).

The influence of specular reflections was more significant and investigated using a modified goniometric setup. The samples were placed in a position comparable to the final aircraft setup and the assemblies were again rotated in front of the lamp. In a narrow range of incidence angles, specularly reflected radiation stroke the receiver. By normalization with the spectra obtained at normal incidence, reflection-induced relative enhancements $Z_{\mathrm{p,R}}$ were obtained. Figure S6 shows the results for the white HALO flange and the black Zeppelin foil in two directions each with respect to the flight direction. For the black foil enhancements are expectedly small and similar in both directions with the small difference probably caused by the production flow path of the foil. In the case of HALO, the differences were more pronounced because in the lateral direction the flange is curved similar to the HALO fuselage. In contrast to the diffuse reflection, no significant wavelength dependence of the $Z_{\mathrm{p,R}}$ was found for the white paint of HALO probably because the specular reflection is

Figure S7. Photograph of the HALO top fuselage with instrument apertures. Left: Instrument plate installed in a larger, black adapter flange for the FLV configuration. Right: standard aperture used for FLT and FLN configurations (closed with a white blind flange).

caused by an outer coating. The finally derived $Z_{\mathrm{p,R}}$ correspond to averages in a 320–420 nm range. Because the situation on the aircraft could not be reproduced exactly in the laboratory, we estimate a 20% uncertainty for the respective angle-dependent enhancements. The use of greater, black-anodized aircraft flanges on HALO as shown in Fig. S7 effectively prevented these fuselage reflections for the HALO-FLV configuration (Sect. 2.1, main text).

S2.4 4 π aircraft configurations

Figures S8 and S10 show contour plots of total relative angular sensitivities $Z_{\mathrm{p}}^{\mathrm{T}}$ of the HALO configurations FLN and FLV for a wavelength of 400 nm. Compared to Fig. 6 in the main text showing the same data for the third configuration (FLT), there are some differences in a range $80° \leq \vartheta \leq 100°$ that mainly come from different positions of the receivers on the bottom fuselage (FLN) and different fuselage reflections (FLV).

The azimuthal averages in Figs. S9 and S11 show corresponding differences near the horizon which, in a first assessment, result in correction factors of 1.055 and 1.016 for isotropic 400 nm radiance distributions for FLN and FLV configurations, respectively, compared to 1.045 for FLT. The differences are small but not negligible and can be more pronounced under real atmospheric conditions.

The $Z_{\mathrm{p}}^{\mathrm{T}}$ results for the Zeppelin are shown in Figs. S12 and S13. For the Zeppelin, surface reflections have a minor influence. The strong enhancement of $Z_{\mathrm{p}}^{\mathrm{T}}$ in the upper hemisphere is caused by the cross-talk of the bottom receiver. The integral of the $\sin(\vartheta) \times Z_{\mathrm{p}}^{\mathrm{T}}$ curve in panel (b) of Fig. S13 correspond to a correction factor of 1.116 for an isotropic radiance distribution at 400 nm. This enhanced value can be attributed to cross-talk effects and $Z_{\mathrm{p}}^{\mathrm{T}}$ values exceeding unity, most significantly in the lower hemisphere.

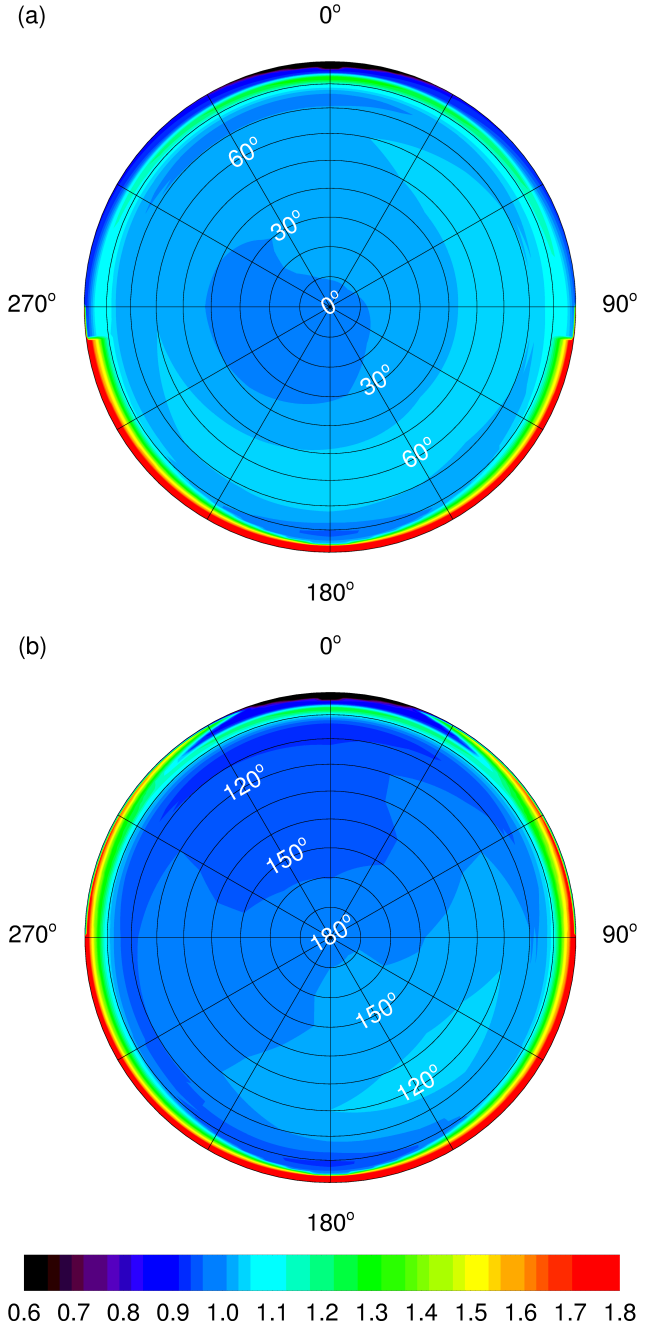

Figure S8. Contour plots of total relative angular sensitivities $Z_{\mathrm{p}}^{\mathrm{T}}$ of the HALO-FLN 4π receiver combination at 400 nm (top views). (a) Upper hemisphere, (b) lower hemisphere. An azimuth angle of 0° corresponds to the flight direction. For the FLN configuration field of view and fuselage reflection effects are considered. Wing box effects on the lower fuselage are missing because the bottom receiver was installed in the aircraft rear section.

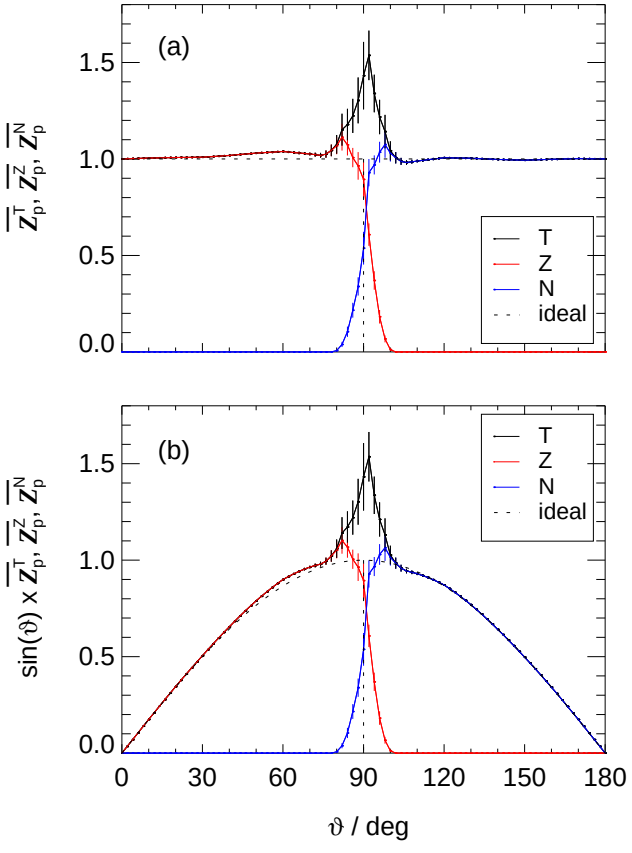

Figure S9. (a) Azimuthal averages of relative total angular sensitivities $Z_{\mathrm{p}}^{\mathrm{T}}$ (T) shown in Fig. S8 (HALO-FLN) with contributions $Z_{\mathrm{p}}^{\mathrm{Z}}$ (Z) and $Z_{\mathrm{p}}^{\mathrm{N}}$ (N) of top and bottom receivers, respectively, for a wavelength of 400 nm (2° interpolations). Error bars represent estimated mean uncertainties not covering azimuthal variabilities. The relative sensitivities of ideal 2π and 4π receivers are shown for comparison (dashed lines). (b) The same data as in (a) but multiplied with $\sin(\vartheta)$ to account for the ϑ dependence of solid-angle contributions.

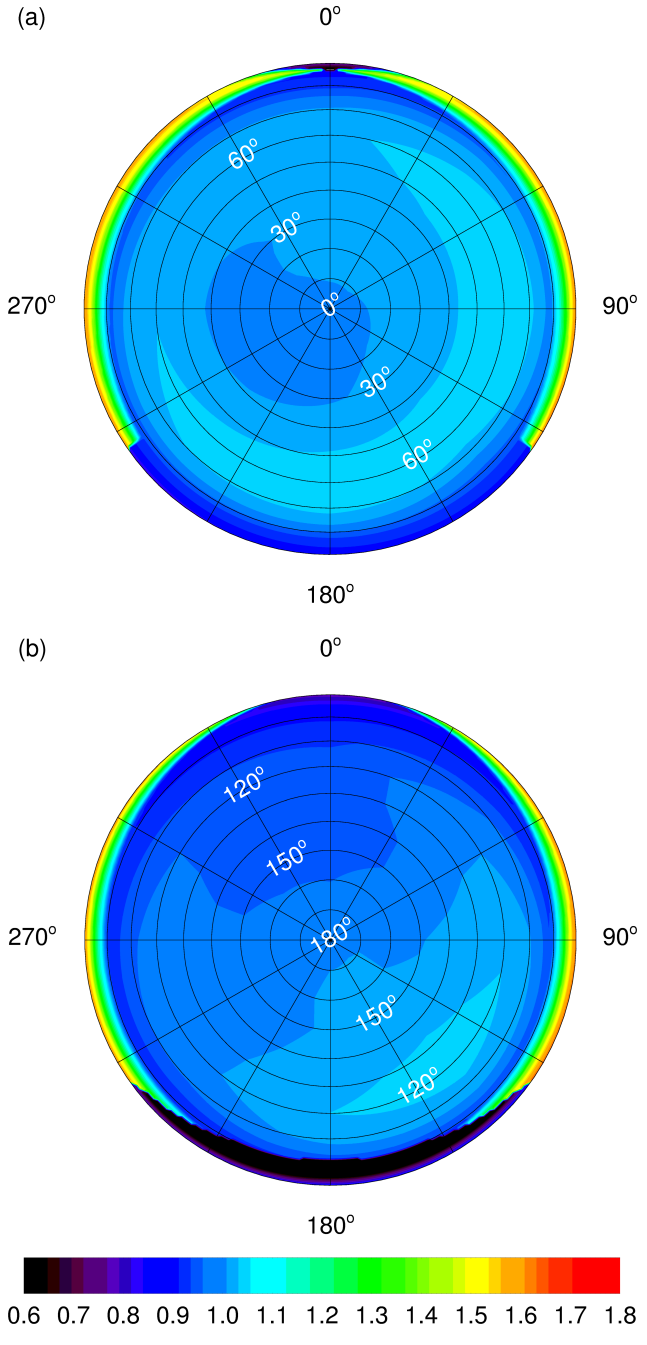

Figure S10. Contour plots of total relative angular sensitivities $Z_{\mathrm{p}}^{\mathrm{T}}$ of the HALO-FLV 4π receiver combination at 400 nm (top views). (a) Upper hemisphere, (b) lower hemisphere. An azimuth angle of 0° corresponds to the flight direction. For the FLV configuration field of view effects are considered including the influence of the wing box on the lower fuselage causing missing cross-talk in panel (a) and dark areas in panel (b) in rearward directions. No fuselage reflections were considered because receivers were installed in large black-anodized aircraft flanges.

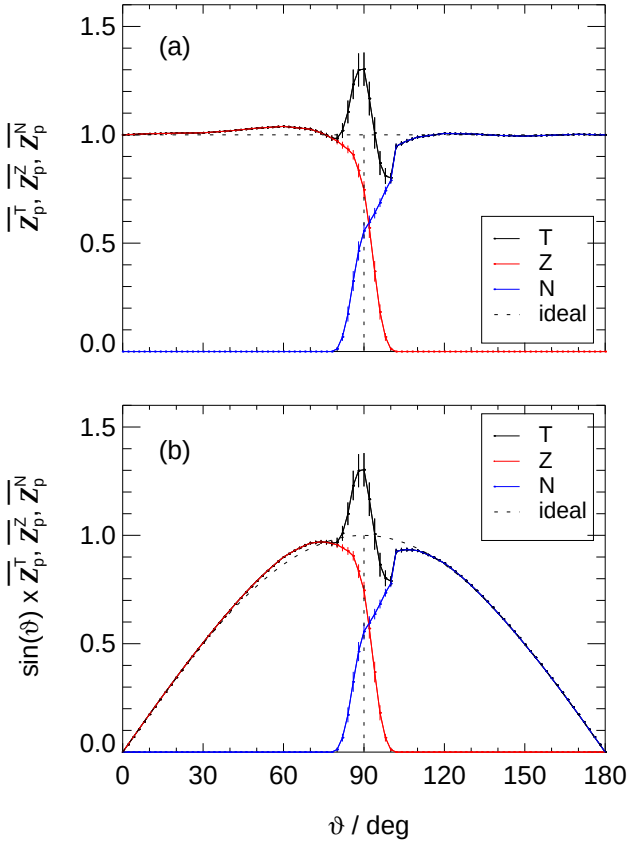

Figure S11. (a) Azimuthal averages of relative total angular sensitivities $Z_{\mathrm{p}}^{\mathrm{T}}$ (T) shown in Fig. S10 (HALO-FLV) with contributions $Z_{\mathrm{p}}^{\mathrm{Z}}$ (Z) and $Z_{\mathrm{p}}^{\mathrm{N}}$ (N) of top and bottom receivers, respectively, for a wavelength of 400 nm (2° interpolations). Error bars represent estimated mean uncertainties not covering azimuthal variabilities. The relative sensitivities of ideal 2π and 4π receivers are shown for comparison (dashed lines). (b) The same data as in (a) but multiplied with $\sin(\vartheta)$ to account for the ϑ dependence of solid-angle contributions.

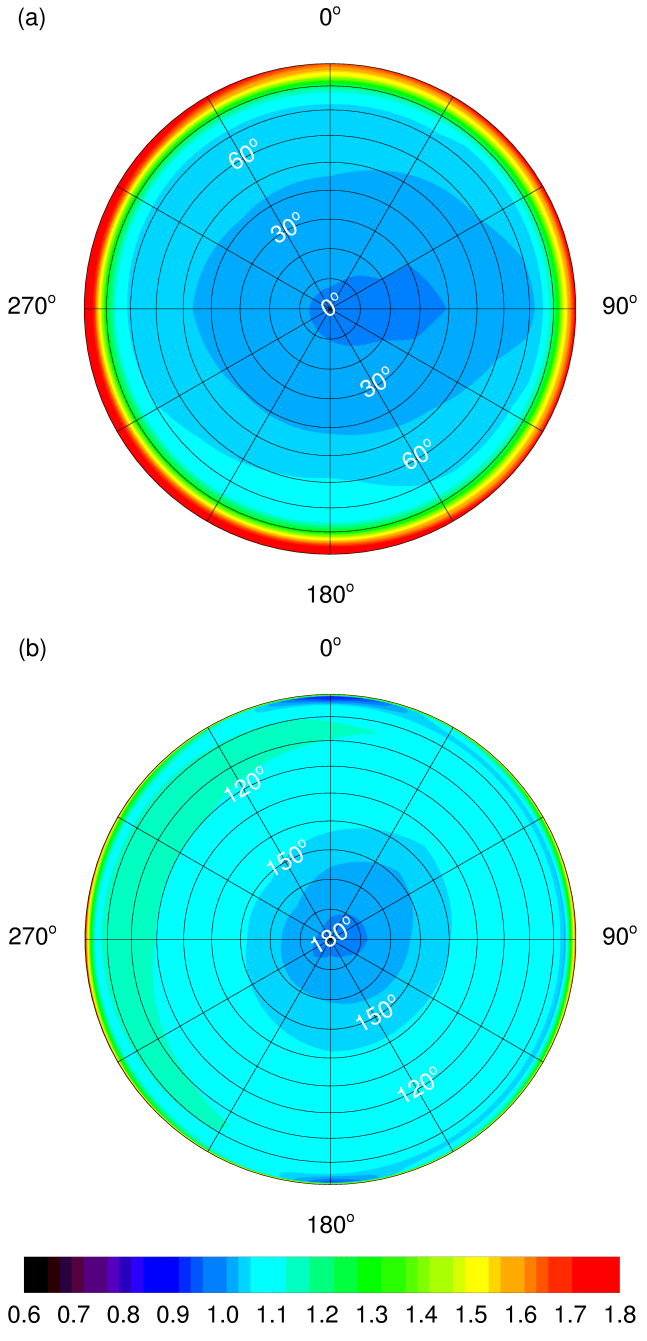

Figure S12. Contour plots of total relative angular sensitivity $Z_{\mathrm{p}}^{\mathrm{T}}$ of the Zeppelin 4π receiver combination in the upper hemisphere (a) and the lower hemisphere (b) at 400 nm (top views). An azimuth angle of 0° corresponds to the flight direction. Zeppelin field of view effects are included as well as black foil fuselage reflections affecting the top receiver. The overestimation in the upper hemisphere is mainly caused by a poor field of view restriction of the bottom receiver.

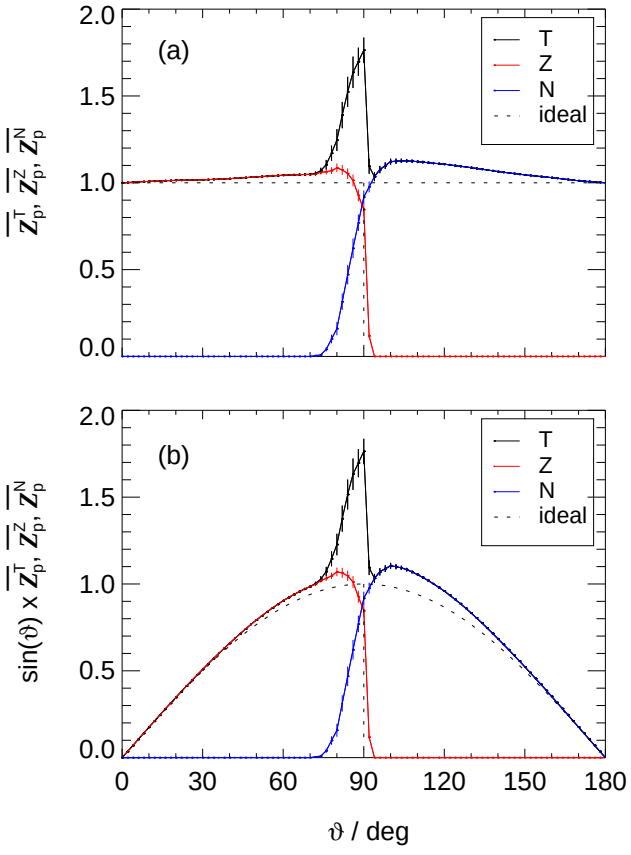

Figure S13. (a) Azimuthal averages of relative total angular sensitivities $Z_{\mathrm{p}}^{\mathrm{T}}$ (T) shown in Fig. S12 (Zeppelin) with contributions $Z_{\mathrm{p}}^{\mathrm{Z}}$ (Z) and $Z_{\mathrm{p}}^{\mathrm{N}}$ (N) of top and bottom receivers, respectively, for a wavelength of 400 nm (2° interpolations). Error bars represent estimated mean uncertainties not covering azimuthal variabilities. The relative sensitivities of ideal 2π and 4π receivers are shown for comparison (dashed lines). (b) The same data as in (a) but multiplied with $\sin(\vartheta)$ to account for the ϑ dependence of solid-angle contributions.

S3 Radiative transfer calculations – Additional information and examples

S3.1 Clouds

For the low- and medium-level St and As layers (water clouds) an effective droplet radius (r_{eff}) of 7 μm was chosen as an intermediate between typical continental and marine clouds (Miles et al., 2000). Assuming an extinction efficiency of the cloud droplets of 2, the liquid water content (LWC) was selected to produce a COD of 25 according to the following equation:

$$\mathrm{COD} \approx \frac{3\ \mathrm{LWP}}{2\ \rho_{\mathrm{l}} r_{\mathrm{eff}}} \tag{S7}$$

Here ρ_l is the density of liquid water ($\approx 1\times10^6$ g m^{-3}) and LWP is the liquid water path. In the simplified cloud cases considered here, the LWPs of about 120 g m^{-2} correspond to the products of the cloud depths (200 m (St), 400 m (As)) and the liquid water contents (LWC) (Table 2, main text).

The altitude and geometrical thickness of the Cs layer was chosen based on a climatology of cirrus clouds for mid-latitude conditions (Sassen and Comstock, 2001). The effective ice particle radius of 20 μm is in the range of typical values (Krämer et al., 2009). In the libRadtran model the shape of the ice crystals was implemented as solid columns with parameterized optical properties (Yang et al., 2013) and the ice water content (IWC) was adjusted to result in a cloud optical depth (COD) of about 1, again roughly representing climatological values (Sassen and Comstock, 2001).

S3.2 Ground albedo

A typical wavelength dependence of ground albedos of vegetated land was calculated by taking the mean of measured values over grass, stub, oats and rye (Feister and Grewe, 1995). This mean spectral surface albedo was scaled to values of 0.02, 0.04 and 0.07 at 470 nm to represent low, mean and high surface albedo spectra over land surfaces as shown in Fig. S14. The reference wavelength of 470 nm was chosen because it corresponds the shortest wavelength band of satellite-derived ground albedos from MODIS which could serve as an input to refine the correction procedure. As additional, limiting cases, wavelength independent ground albedos of 0.0 and 0.8 were used (not shown), the latter representing a maximum value measured over fresh snow (Feister and Grewe, 1995). The spectral albedo of open water is available in the literature above 460 nm and plotted as full line in Fig. S14 (Bowker et al., 1985) with values of around 0.03 at 470 nm. For shorter wavelengths the water albedo was assumed constant. Generally the albedo of water is difficult to determine and dependent on a number of additional parameters like wind speed and the concentration of algae or soil particles. The data shown in Fig. S14 are considered a lower limit (Wendisch et al., 2004).

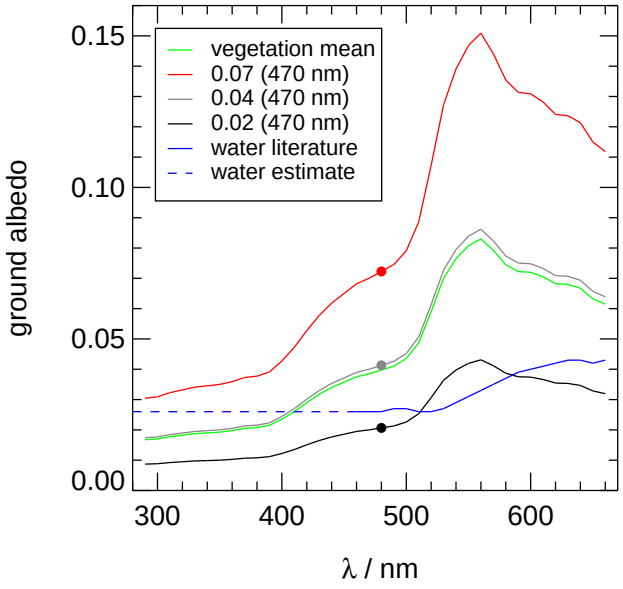

Figure S14. Spectral ground albedos from the literature (vegetation mean) and corresponding scaled cases used in the radiative transfer calculations, as well as open water albedo from the literature and estimated below 450 nm.

S3.3 Aerosol optical depths

Aerosol optical depths of the libRadtran default aerosol are plotted in Fig. S15 as a function of wavelength (full green line). The AODs were scaled to values of 0.03, 0.2 and 1.5 at 550 nm to represent clean remote, standard and polluted conditions. The reference wavelength of 550 nm was chosen because it is most commonly used to characterize aerosol optical depths. The wavelength dependence of the default AOD closely follows a simple relationship:

$$\mathrm{AOD}_\lambda \approx \mathrm{AOD}_{550} \times 550 \times (\lambda/\mathrm{nm})^{-1} \tag{S8}$$

(dashed green line) which corresponds to an Angström exponent of 1.0.

The altitude dependence of the aerosol optical depth (scaled to 0.2 at 550 nm) is shown in Fig. S16 for selected wavelengths indicating a strong decrease with altitude. More than half of the aerosol column AOD is located at altitudes below 2 km.

S3.4 Radiance distributions

Figures S17–S22 show examples of spectral radiance distributions for 400 nm in two representations for direct comparison with Figs. 8 and 9 in the main text. Figures S17 and S18 demonstrate the strong influence of an underlying As cloud layer with a high cloud optical depth of around 25. Total actinic flux density is enhanced by a factor of 1.7 compared to clear-sky conditions. The relative contributions of direct, diffuse downward and diffuse upward radiation to spectral

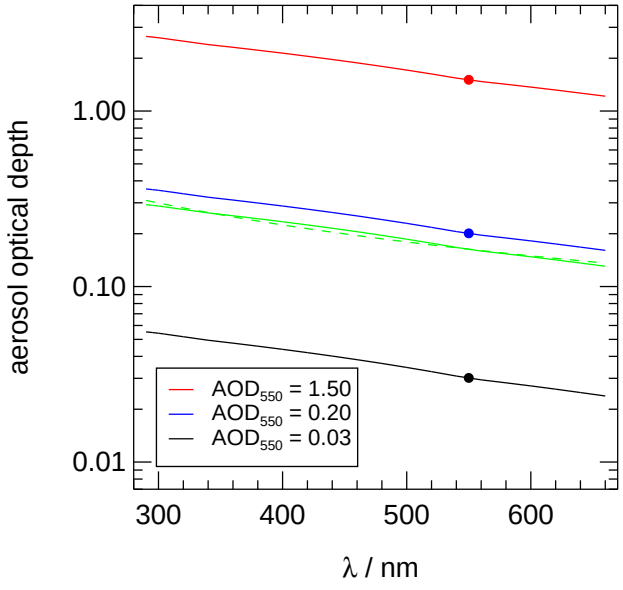

Figure S15. AOD wavelength dependence of the libRadtran default aerosol (green) and scaled data used in the radiative transfer calculations matching AOD_{550} of 0.03, 0.2 and 1.5 as indicated. The dashed green line is a calculation based on the default AOD_{550} and an Angström exponent of 1.0.

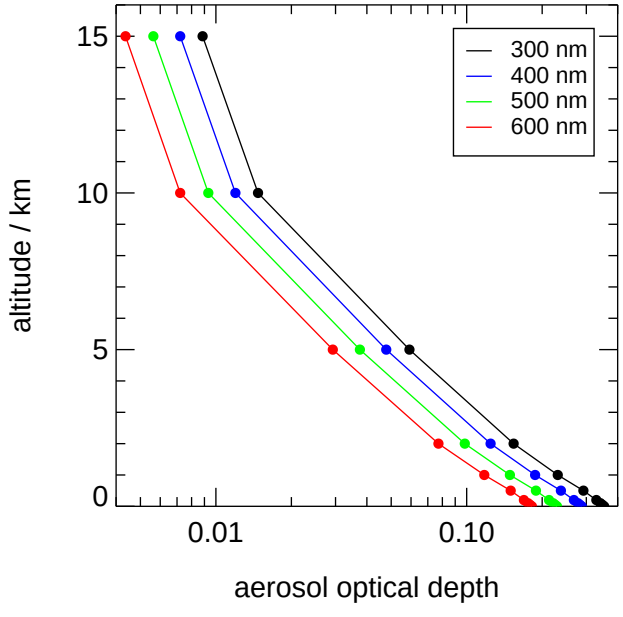

Figure S16. AOD altitude dependence of the libRadtran default aerosol for selected wavelengths after scaling AOD_{550} to 0.2. Symbols indicate model altitudes.

actinic flux density are 0.30, 0.23 and 0.47, respectively. Note the glory- and rainbow phenomenons in the lower hemisphere opposite the sun.

Figures S19 and S20 show a second clear-sky example at a lower altitude of 2 km. Compared to 5 km, total actinic flux densities decreased by about 10% while the contributions of downward and upward diffuse radiances increased and decreased, respectively. The relative contributions of direct, diffuse downward and diffuse upward radiation to the total spectral actinic flux density are 0.47, 0.37 and 0.16, respectively.

Figures S21 and S22 finally illustrate the effects of the As cloud layer below the cloud at an altitude of 2 km. Total actinic flux density is strongly decreased by a factor of 0.38 compared to clear-sky conditions. The relative contributions of direct, diffuse downward and diffuse upward radiation to spectral actinic flux density are 0.00, 0.84 and 0.16, respectively.

S3.5 Data availability

For each atmospheric scenario, altitude and solar zenith angle, the libRadtran calculations were done for 23 wavelengths and 91 azimuth angles (0–180°) simultaneously, though only for a single polar angle of incidence. Consequently, a very large number of input and output files (≈400000) were created and processed automatically. Examples of input files (and output files) for each cloud case and other input data are available in the online material (Bohn, 2022). To provide the model data for other users in a manageable and compact form, all spectral radiances for a given altitude and atmospheric scenario were put together in a single netcdf file, including spectral actinic flux densities. For the sake of completeness, spectral irradiances were also included for users aiming at corrections for cosine receivers. The three letter/figure codes for the filenames were defined as follows. Cloud cases: CLR, CIR, AST, STR. Altitudes: 000, 00Z, 001, 002, 005, 010, 020, 035, 050, 100, 110, 120 and 150 (AGL/km = 0.00, 0.05, 0.1, 0.2, 0.5, 1.0, 2.0, 3.5, 5.0, 10.0, 11.0, 12.0 and 15.0). Ground albedos: A00, A02, A03, A04, A07 and A80 (A_{470} = 0.00, 0.02, 0.03 (water), 0.04, 0.07 and 0.80 (snow)). Aerosol optical depths: T00, T0Z, T02 and T15 (AOD_{550} = 0.00, 0.03, 0.20 and 1.50). For example, the filename AST_010_A04_T02.nc denotes an AST cloud case, an altitude of 1 km, a ground albedo of 0.04 at 470 nm and an AOD of 0.02 at 550 nm.

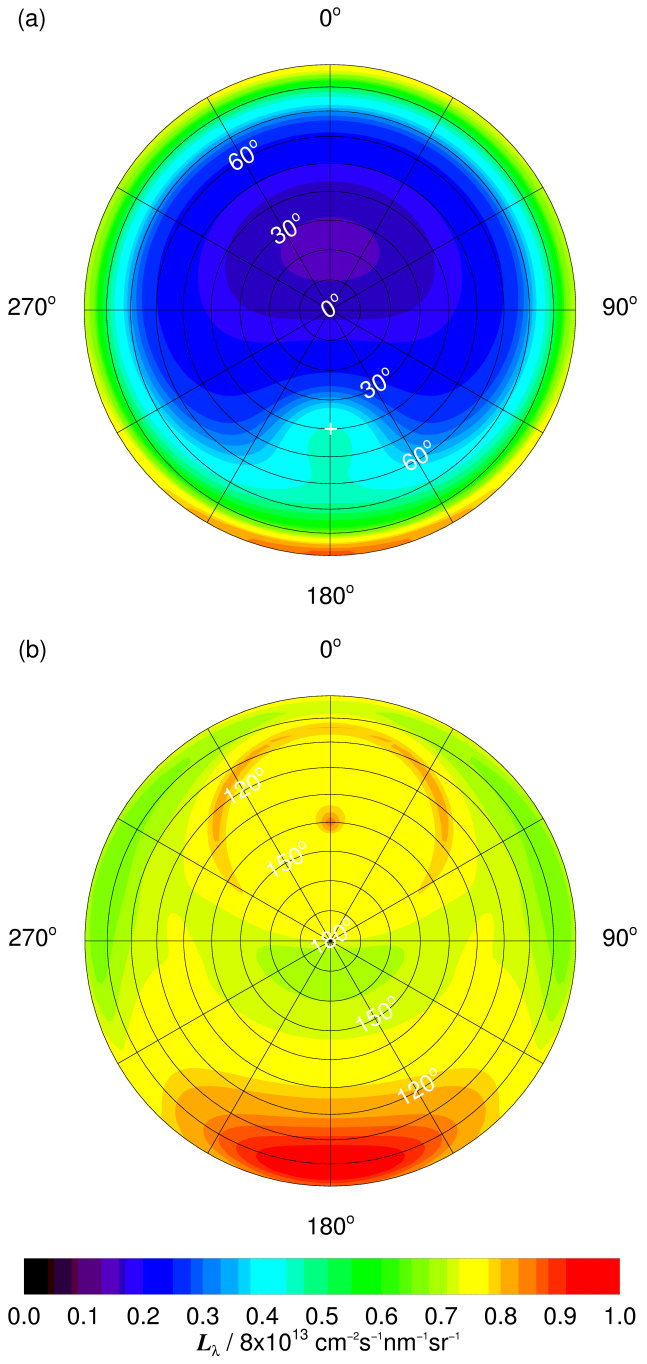

Figure S17. Contour plots of modelled diffuse spectral radiance distributions for a wavelength of 400 nm at an altitude of 5 km, 1.3 km above an As cloud layer under otherwise the same conditions as in Fig. 8, main paper. (a) Downward spectral radiance. (b) Upward spectral radiance. The position of the sun is indicated by the white cross in panel (a).

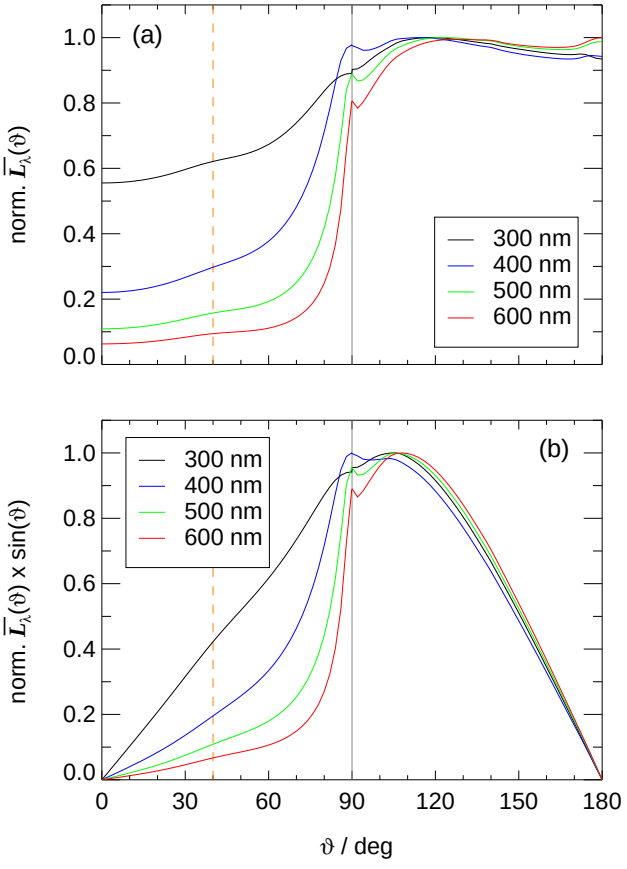

Figure S18. (a) Polar angle dependence of normalized, azimuthal mean diffuse spectral radiances for different wavelengths for the atmospheric conditions of Fig. S17. (b) Azimuthal mean spectral radiances as in panel (a) but weighted with sin(ϑ). The vertical grey line indicates the horizon, the dashed orange line the position of the sun. Direct sun contribution to spectral actinic flux densities for this scenario are 0.23 (300 nm), 0.30 (400 nm), 0.38 (500 nm) and 0.41 (600 nm). Compare to Fig. 9, main paper

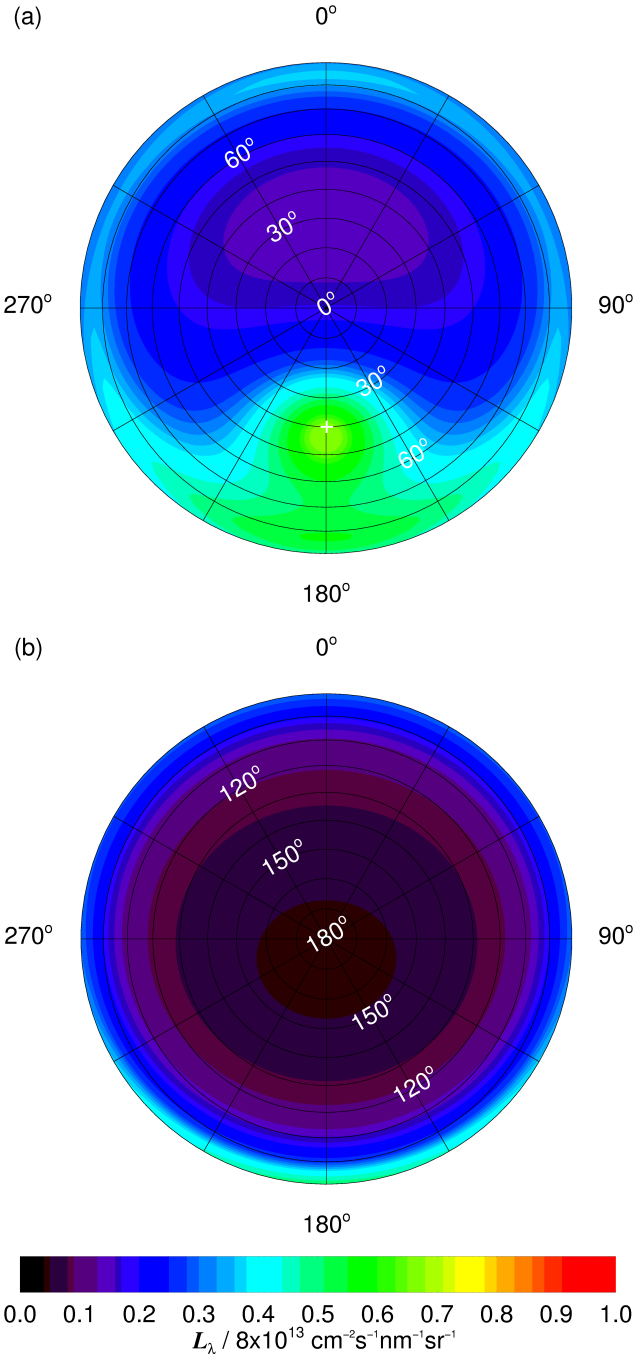

Figure S19. Contour plots of modelled diffuse spectral radiance distributions for a wavelength of 400 nm at an altitude of 2 km under clear-sky conditions at solar zenith and azimuth angles of 40° and 180°, respectively. (a) Downward spectral radiance. (b) Upward spectral radiance. The position of the sun is indicated by the white cross in panel (a). In this example, ground albedos were scaled to 0.04 at 470 nm and aerosol optical depths to 0.2 at 550 nm. The colour scale was chosen for better comparability with Fig. S17.

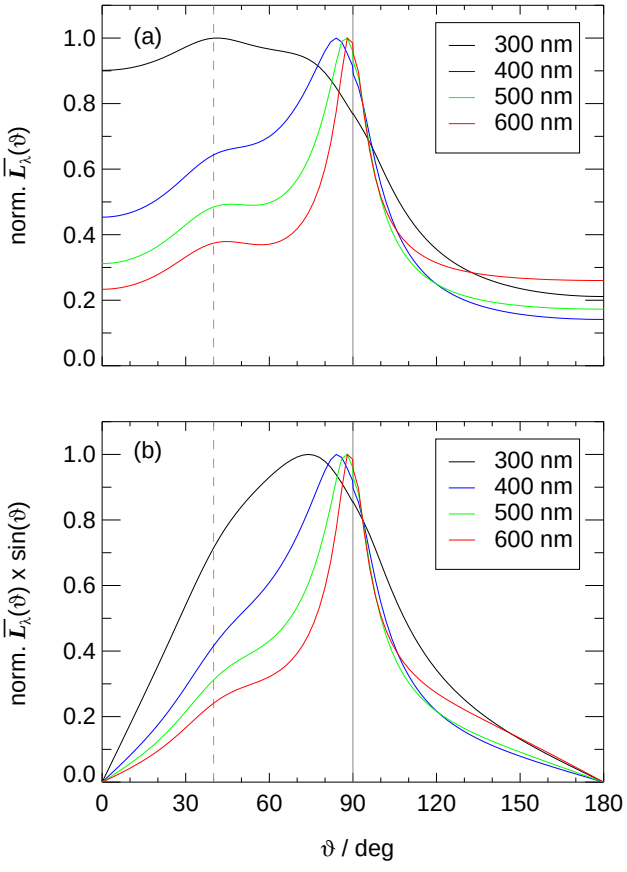

Figure S20. (a) Polar angle dependence of normalized, azimuthal mean diffuse spectral radiances for different wavelengths for the atmospheric conditions of Fig. S19. (b) Azimuthal mean spectral radiances as in panel (a) but weighted with sin(ϑ). The vertical grey line indicates the horizon, the dashed orange line the position of the sun. Direct sun contribution to spectral actinic flux densities for this scenario are 0.27 (300 nm), 0.48 (400 nm), 0.62 (500 nm) and 0.68 (600 nm).

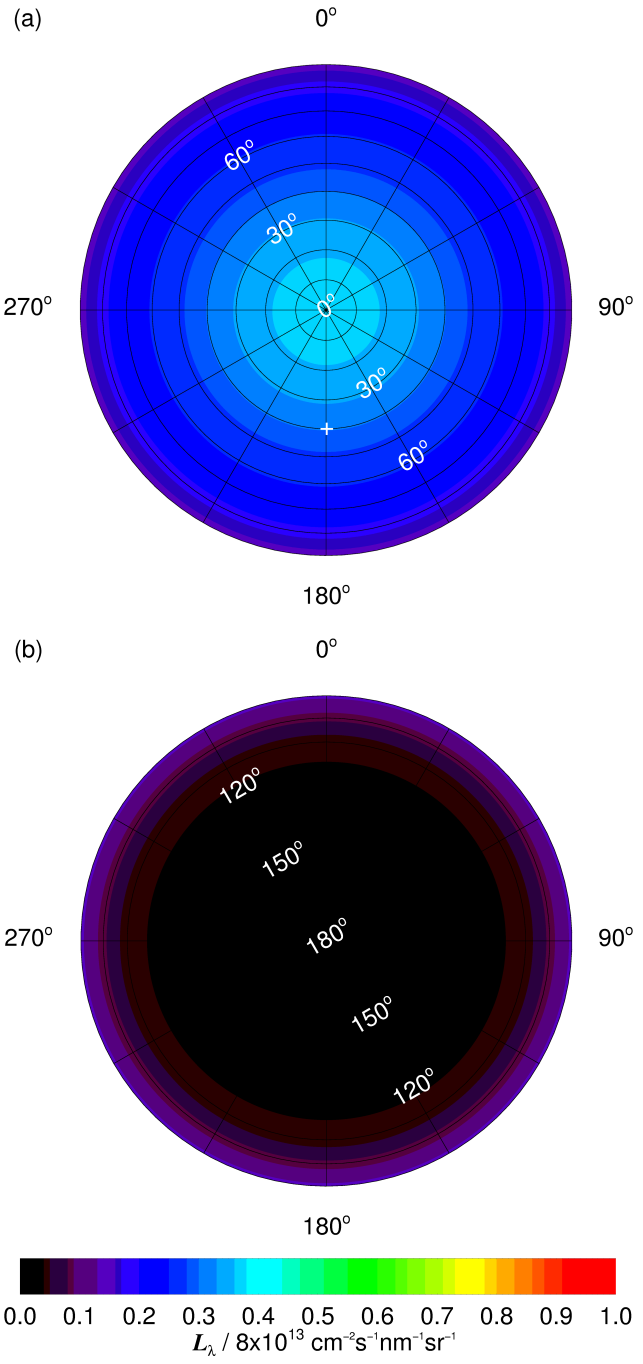

Figure S21. Contour plots of modelled diffuse spectral radiance distributions for a wavelength of 400 nm at an altitude of 2 km, 1.3 km below an As cloud layer under otherwise the same conditions as in Fig. S19. (a) Downward spectral radiance. (b) Upward spectral radiance. Note that the downward spectral radiance increases strongly towards smaller polar angles.

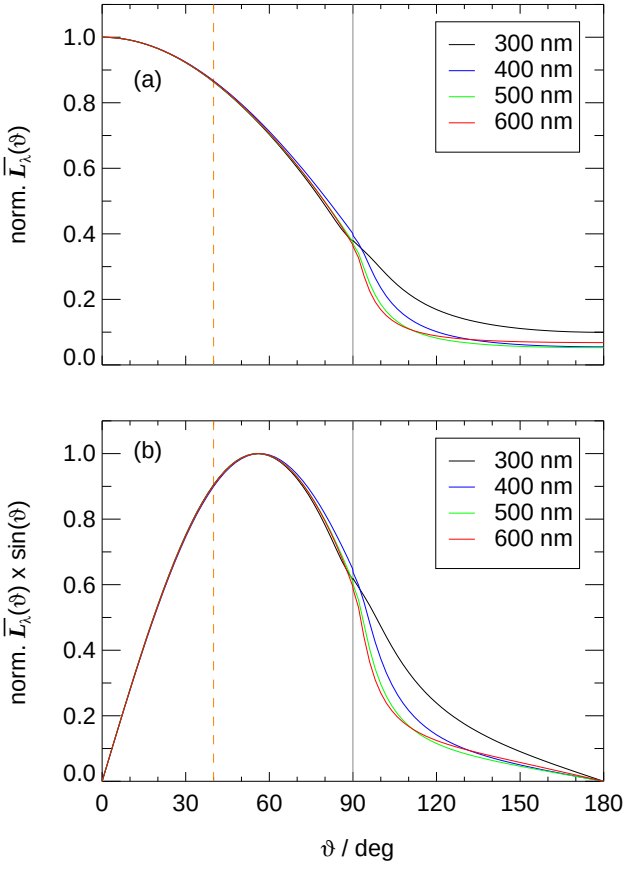

Figure S22. (a) Polar angle dependence of normalized, azimuthal mean diffuse spectral radiances for different wavelengths for the atmospheric conditions of Fig. S21. (b) Azimuthal mean spectral radiances as in panel (a) but weighted with sin(ϑ). The vertical grey line indicates the horizon, the dashed orange line the position of the sun. Direct sun contribution to spectral actinic flux densities for this scenario are zero for all wavelenghts.

Table S1. Atmospheric model scenarios for the evaluation of correction functions for the airborne platforms HALO and Zeppelin, and a ground station. The letter T (turbidity) denotes three scenarios with different aerosol optical depth cases at standard ground albedo (A_{470} = 0.04), the letter A (albedo) four additional scenarios with different ground albedo cases at standard aerosol optical depth (AOD_{550} = 0.2) with 23 wavelengths and 12 solar zenith angles for each scenario.

Altitude (km)			Cloud case			
HALO	Zeppelin	Ground	Cl	Cs	As	St[a]
–	–	0.00	T, A	T, A	T, A	–
–	0.05		T, A	T, A	T, A	–
–	0.10		T, A	T, A	T, A	–
0.20	0.20		T, A	T, A	T, A	T
0.50	0.50		T, A	T, A	T, A	T
1.0	1.0		T, A	T, A	T, A	T
2.0	2.0		T, A	T, A	T, A	T
3.5[b]			–	–	T, A	–
5.0			T, A	T, A	T, A	T
10			T, A	T, A	T, A	T
11[b]			–	T, A	–	–
12[c]			–	T, A	–	–
15			T, A	T, A	T, A	T

[a] Not considered for the Zeppelin. [b] In-cloud altitude for a specific cloud case. [c] Cloud top altitude for a specific cloud case.

S4 Modelled correction functions – Additional examples

Figures S23–S25 show examples of correction functions $Z^{\mathrm{G}}_{\mathrm{H}}$ for ground-based measurements of downward spectral actinic flux densities with the HALO bottom, Zeppelin top and Zeppelin bottom receivers for different cloud cases as a function of solar zenith angles under the same conditions as in Fig. 10 of the main paper (HALO top receiver). There are significant differences between the different receivers which originate from the receiver-specific differences of the angular sensitivities (Figs. 4 and 5, main paper and Figs. S4 and S5).

All corrections derived for the different atmospheric scenarios and receiver configurations are available for download in files compatible with the radiance distributions (Bohn, 2022). The configurations can be inferred from the filenames: GRD refers to corrections for the four receivers on the ground, ZEPP_FLT to the Zeppelin configuration, and HALO_FLT, HALO_FLN and HALO_FLV refer to the three HALO configurations. However, it should be noted that these corrections are specific for the receivers and aircraft/ground configurations used in this work and should not be applied otherwise.

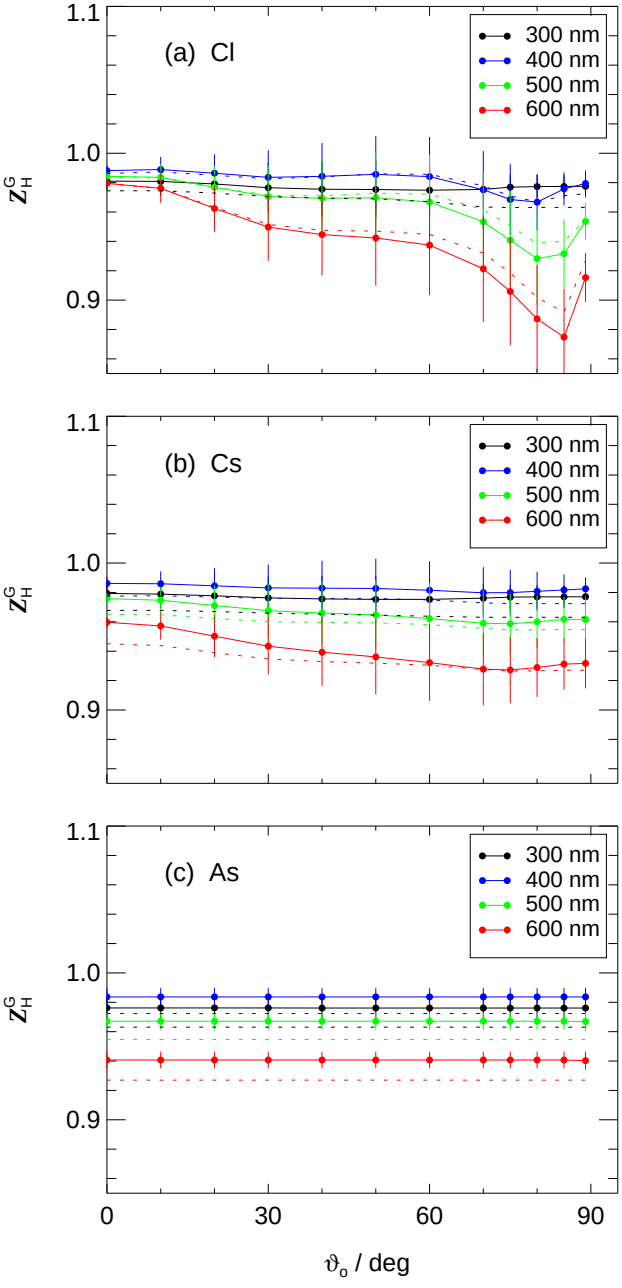

Figure S23. Modelled correction functions $Z^{\mathrm{G}}_{\mathrm{H}}$ for ground-based measurements of downward spectral actinic flux densities with the HALO bottom receiver as a function of solar zenith angle for selected wavelengths. Corrections apply to standard aerosol load and ground albedos at different cloud cases. Upper panel (a): clear-sky (Cl); middel panel (b): Cs cloud layer; lower panel (c): As cloud layer. Dashed lines show results assuming isotropic distributions of downward diffuse spectral radiances for comparison.

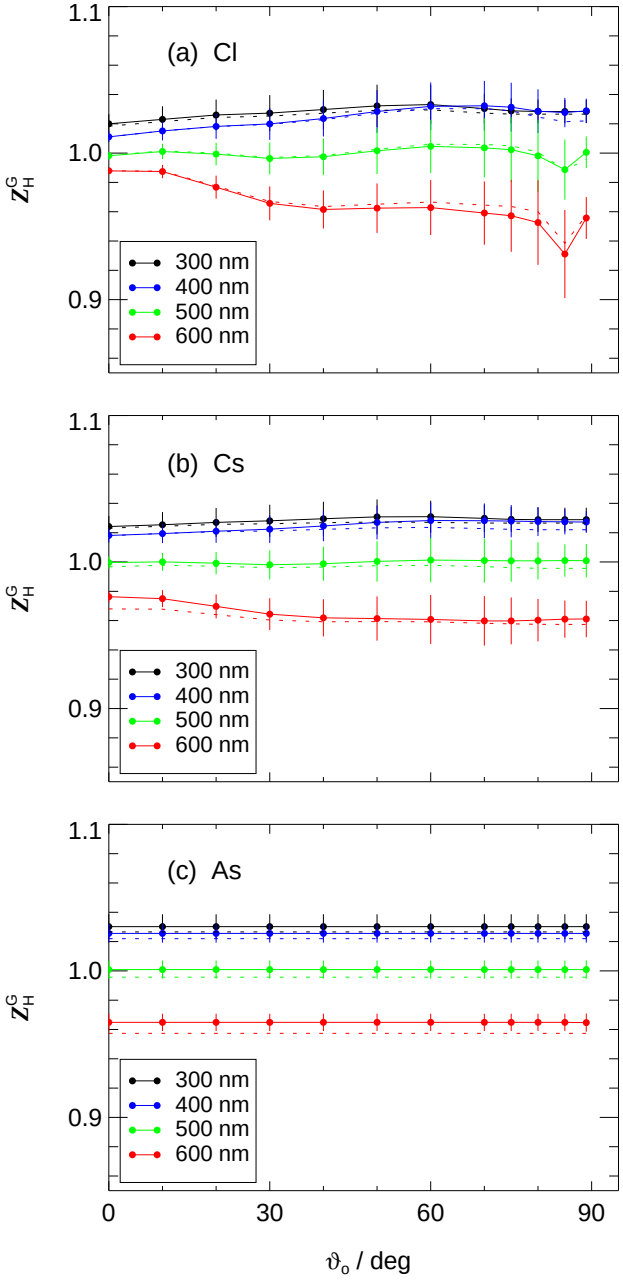

Figure S24. Modelled correction functions $Z_{\mathrm{H}}^{\mathrm{G}}$ for ground-based measurements of downward spectral actinic flux densities with the Zeppelin top receiver as a function of solar zenith angle for selected wavelengths and different cloud cases as in Fig. S23.

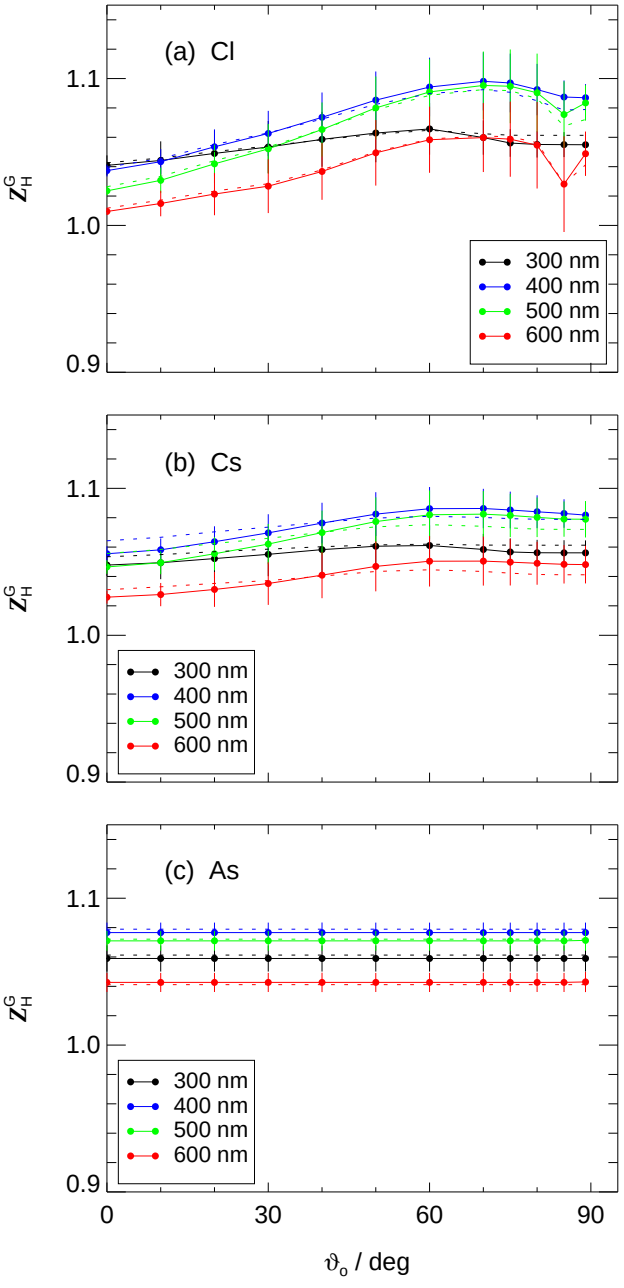

Figure S25. Modelled correction functions $Z_{\mathrm{H}}^{\mathrm{G}}$ for ground-based measurements of downward spectral actinic flux densities with the Zeppelin bottom receiver as a function of solar zenith angle for selected wavelengths and different cloud cases as in Fig. S23.

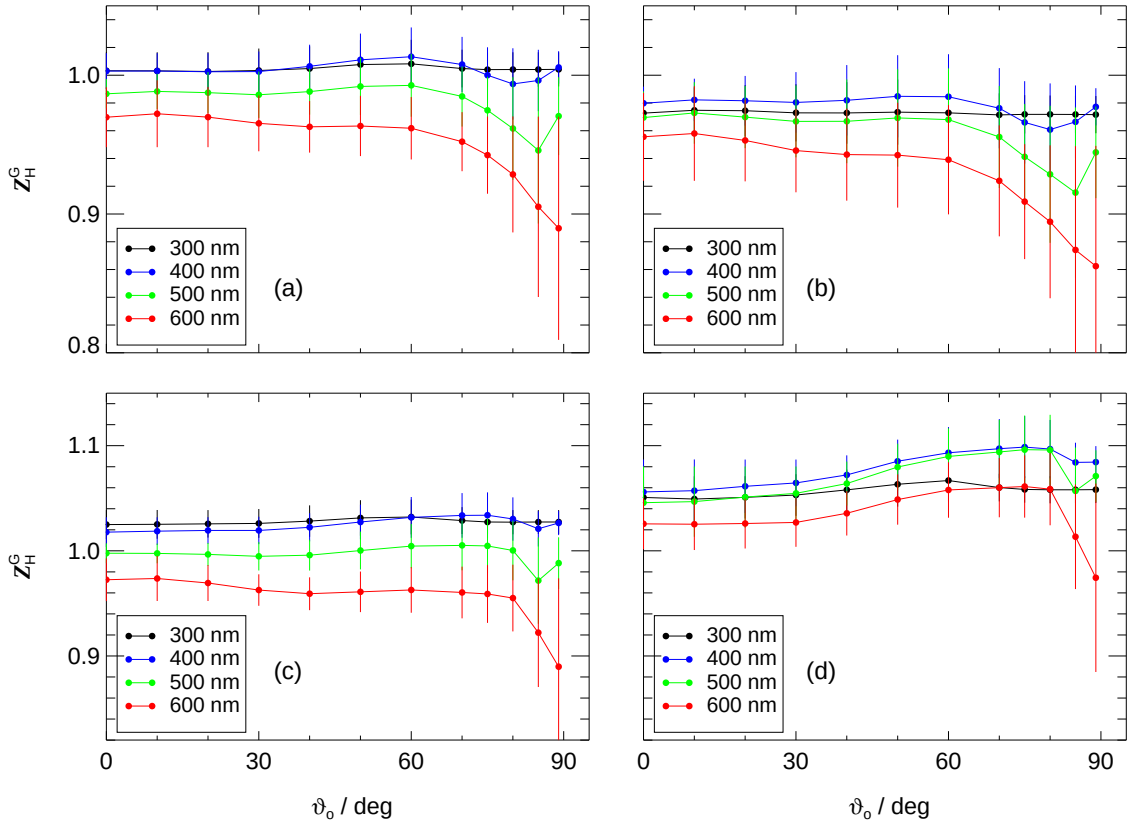

Figure S26. Final ground station correction functions $Z_{\mathrm{H}}^{\mathrm{G}}$ of the four receivers HALO top (a), HALO bot (b), Zeppelin top (c) and Zeppelin bot (d) for selected wavelengths as a function of solar zenith angle. Uncertainties cover the model results and uncertainties of all atmospheric scenarios.

S5 Final corrections for ground-based measurements

Figure S26 shows the final $Z_{\mathrm{H}}^{\mathrm{G}}$ for selected wavelengths as a function of solar zenith angle for the four receivers investigated in this work. Uncertainties cover all relevant atmospheric scenarios. Corrections for other wavelengths and solar zenith angles can be derived by linear interpolations of corrections and uncertainties based on the wavelengths and solar zenith angles used in the model calculations. The corrections apply to a height above ground of zero at mean sea level. As mentioned in the main text, corrections are very similar for a ground elevation of 1 km. For measurement sites with ground elevations well above 1 km it is recommended to perform site-specific radiative transfer calculations rather than using the sea level data provided in this work.

S6 Parametrizations - Additional examples

Figure S27 shows examples of modelled in-cloud corrections together with altitude-interpolated parametrizations of all other scenarios for the Cs layer at 11 km (upper panel) and the As layer at 3.5 km (lower panel). The in-cloud corrections at 11 km are covered by the parametrizations, at least in the UV range and small solar zenith angles. At larger wavelengths and solar zenith angles, parameterized corrections are biased low, mainly for the upward spectral actinic flux densities, because for 15 km no below-cloud scenario was included (see Sect. 5.3.2, main text). At 3.5 km altitude, maximum deviations from the parametrizations remain below about 2% and within the uncertainty limits.

Figure S29 shows corrections obtained for ozone columns of 200 DU and 400 DU compared to the parametrizations derived for 300 DU for altitudes of 10 km and 1 km (test calculations at standard ground albedos and aerosol optical depths). Although for 10 km altitude (upper panel) the Φ_{m} show some dependence on ozone columns, the corrections remain in the range of the uncertainties of the parametrizations. For other wavelengths in the UV-B range similar results were obtained while for wavelengths >320 nm corrections become independent of ozone columns. At 1 km altitude (lower panel) the differences are insignificant.

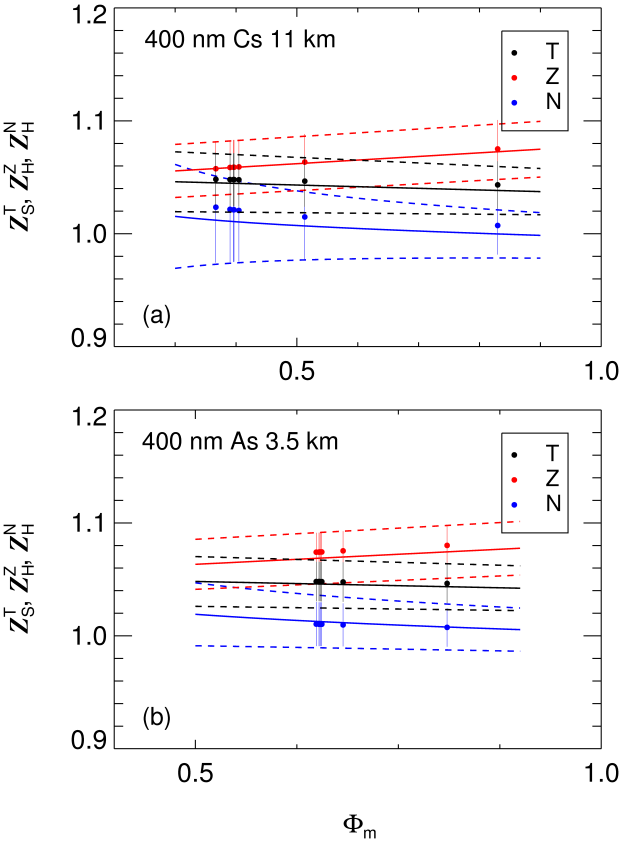

Figure S27. Modelled correction functions $Z_{\mathrm{S}}^{\mathrm{T}}$ (T), $Z_{\mathrm{H}}^{\mathrm{Z}}$ (Z) and $Z_{\mathrm{H}}^{\mathrm{N}}$ (N) for HALO under in-cloud conditions as a function of Φ_{m} in cloud layers Cs at 11 km (a) and As at 3.5 km (b) for a wavelength of 400 nm and a solar zenith angle of 40° (7 scenarios each at different aerosol optical depths and ground albedos). Full and dashed lines of the same colour show the altitude-interpolated parametrizations of the correction functions and their uncertainty ranges, respectively, which cover the in-cloud results. Data apply to a solar heading angle of 90° in this example.

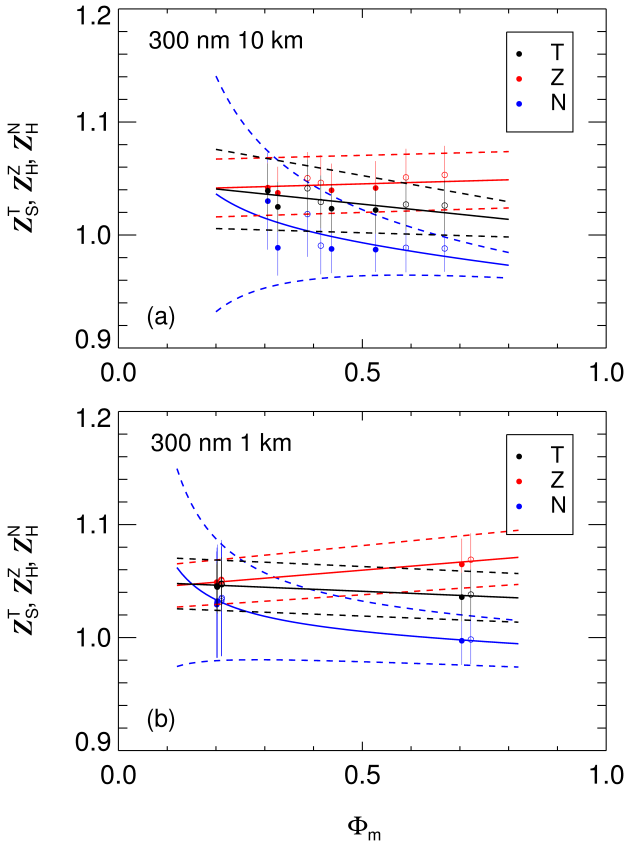

Figure S28. Modelled correction functions Z_S^T (T), Z_H^Z (Z) and Z_H^N (N) for HALO as a function of Φ_m at 10 km (a) and 1 km (b) for a wavelength of 300 nm and a solar zenith angle of 40° (CLR, CIR, AST and STR cloud cases each at standard aerosol and ground albedos). Open symbols show results for total ozone columns of 200 DU, filled symbols for 400 DU. Full lines and dashed lines show the 300 DU parametrizations of the correction functions and their uncertainty ranges, respectively, which cover the 200 DU and 400 DU results. Data apply to a solar heading angle of 90° in this example.

S7 Correction procedure

In order to derive corrections for measured airborne data, a four-step procedure was applied. First, the actinic flux density spectra, that were recorded independently in the upper and the lower hemisphere, were synchronized with respect to time and wavelength, using a common 280–660 nm wavelength range with a step size of 1 nm. Second, the experimental Φ_m were calculated for the same wavelengths as used in the model simulations by averaging spectral actinic flux densities over ±5 nm ranges to reduce noise. Third, the parametrization coefficients were interpolated along the flight tracks taking into account solar zenith angles and heights above ground, as well as solar heading angles in the case of HALO. Heights above ground for the Zeppelin were available from on board laser altimeter measurements. For HALO, heights above ground were derived from aircraft GPS altitudes (WGS84), interpolated geoid heights (EGM96) and ground elevations from the ALOS Global Digital Surface Model (AW3D30, Version 3.1)(Takaku et al., 2020). Solar heading angles for HALO were calculated from aircraft heading angles and solar azimuth angles. With the interpolated coefficients and the experimental Φ_m, the corrections and uncertainties were calculated for the wavelengths used in the model simulations. These data were saved for optional consistency checks. Fourth, the corrections and uncertainties were interpolated to the common wavelength grid and applied to the synchronized spectra to obtain corrected total, downward and upward spectral actinic flux densities and corresponding uncertainties. All interpolations are uncomplicated because parametrization coefficients and uncorrected ratios change smoothly with solar zenith angle, heading angle, altitude and wavelength. Besides the uncertainties from the corrections, uncertainties from calibrations and instrument noise were included (Bohn and Lohse, 2017) to determine total uncertainties. In a final step, data were excluded where (i) solar zenith angles were greater than 80°, (ii) aircraft attitudes were greater than 2.5° (HALO) or 5° (Zeppelin), and (iii) the heights above ground were below 200 m (HALO) or 50 m (Zeppelin).

In addition, some further campaign-specific corrections were required for HALO. At large solar zenith angles, shadings of the top receiver from direct sun by other inlets and the tail-unit of the aircraft are possible, dependent on the campaign-specific inlet configuration. Rare periods where such shadings were possible were taken out from the final data sets. These periods were determined based on the known solar zenith and azimuth angles as well as the aircraft headings. For diffuse sky radiation these inlet-induced shading effects were negligible.

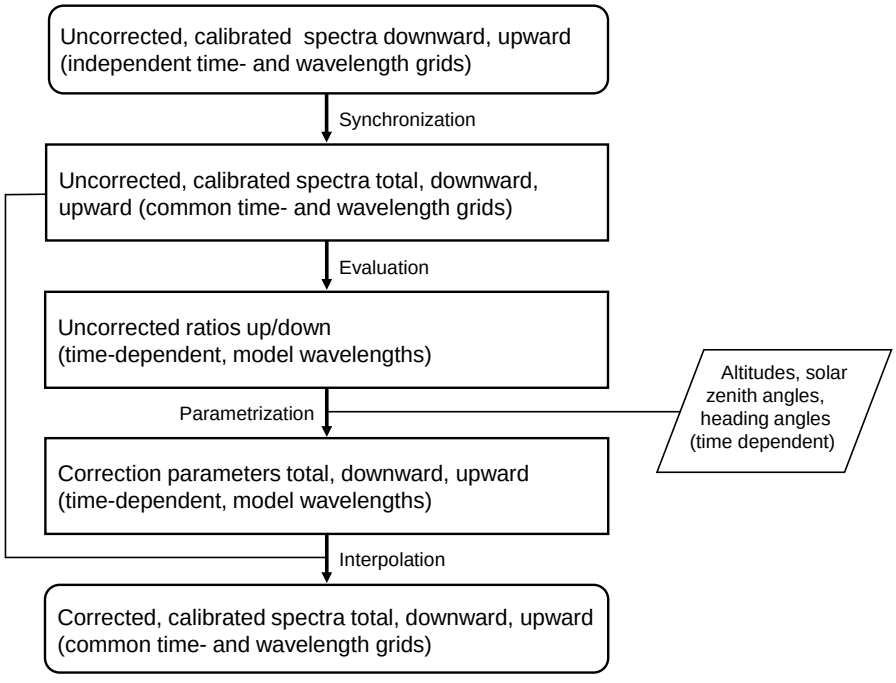

Figure S29. Schematic of data evaluation steps to derive corrections for airborne measurements. More details are given in Sect. S7. The final step of data selection (dependent on platform-specific selection criteria, for example, minimum altitudes, shadings etc.), was omitted.

References

Bohn, B. and Lohse, I.: Calibration and evaluation of CCD spectroradiometers for ground-based and airborne measurements of spectral actinic flux densities, Atmospheric Measurement Techniques, 10, 3151–3174, https://doi.org/10.5194/amt-10-3151-2017, 2017.

Bohn, B.: Replication data for "Optical receiver characterisations and corrections for ground-based and airborne measurements of spectral actinic flux densities", V2, Jülich DATA [data set], https://doi.org/10.26165/JUELICH-DATA/8INBXK, 2022.

Bowker, D. E., Davis, R. E., Myrick, D. L., Stacy, K., and Jones, W. T.: Spectral Reflectances of Natural Targets for Use in Remote Sensing Studies, NASA-Langley, NASA RP-1139, 184 pp., 1985.

Feister, U. and Grewe, R.: Spectral albedo measurements in the UV and visible region over different types of surfaces, J. Photochem. Photobiol., 62, 736–744, https://doi.org/10.1111/j.1751-1097.1995.tb08723.x, 1995.

Krämer, M., Schiller, C., Afchine, A., Bauer, R., Gensch, I., Mangold, A., Schlicht, S., Spelten, N., Sitnikov, N., Borrmann, S., de Reus, M., and Spichtinger, P.: Ice supersaturations and cirrus cloud crystal numbers, Atmospheric Chemistry and Physics, 9, 3505–3522, https://doi.org/10.5194/acp-9-3505-2009, 2009.

Miles, N. L., Verlinde, J., and Clothiaux, E. E.: Cloud Droplet Size Distributions in Low-Level Stratiform Clouds, Journal of the Atmospheric Sciences, 57, 295 – 311, https://doi.org/10.1175/1520-0469(2000)057<0295:CDSDIL>2.0.CO;2, 2000.

Sassen, K. and Comstock, J. M.: A Midlatitude Cirrus Cloud Climatology from the Facility for Atmospheric Remote Sensing. Part III: Radiative Properties, Journal of the Atmospheric Sciences, 58, 2113–2127, https://doi.org/10.1175/1520-0469(2001)058<2113:AMCCCF>2.0.CO;2, 2001.

Takaku, J., Tadono, T., Doutsu, M., Ohgushi, F., and Kai, H.: Updates of 'AW3D30' ALOS Global Digital Surface Model with Other Open Access Datasets, The International Archives of the Photogrammetry, Remote Sensing and Spatial Information Sciences, ISPRS, Vol.XLIII-B4-2020, pp.183–189, https://doi.org/10.5194/isprs-archives-XLIII-B4-2020-183-2020, 2020.

Wendisch, M., Pilewskie, P., Jäkel, E., Schmidt, S., Pommier, J., Howard, S., Jonsson, H., Guan, H., Schroder, M., and Mayer, B.: Airborne measurements of areal spectral surface albedo over different sea and land surfaces, Journal of Geophysical Research-Atmospheres, 109, D08 203, https://doi.org/10.1029/2003JD004392, 2004.

Yang, P., Bi, L., Baum, B. A., Liou, K.-N., Kattawar, G. W., Mishchenko, M. I., and Cole, B.: Spectrally Consistent Scattering, Absorption, and Polarization Properties of Atmospheric Ice Crystals at Wavelengths from 0.2 to 100 μm, Journal of the Atmospheric Sciences, 70, 330–347, https://doi.org/10.1175/JAS-D-12-039.1, 2013.